Polymer-Plastics Technology and Engineering

ISSN: 0360-2559 (Print) 1525-6111 (Online) Journal homepage: http://www.tandfonline.com/loi/lpte20

Mechanical and Dynamic Behavior of Fused Filament Fabrication 3D Printed Polyethylene Terephthalate Glycol Reinforced with Carbon Fibers

M. Mansour, K. Tsongas, D. Tzetzis & A. Antoniadis

POLYMER-PLASTICS TECHNOLOGY AND ENGINEERING
https://doi.org/10.1080/03602559.2017.1419490

Mechanical and Dynamic Behavior of Fused Filament Fabrication 3D Printed Polyethylene Terephthalate Glycol Reinforced with Carbon Fibers

M. Mansour[a], K. Tsongas[b], D. Tzetzis[c], and A. Antoniadis[a]

[a]School of Production Engineering and Management, Technical University of Crete, Chania, Greece; [b]Department of Mechanical Engineering, Aristotle University of Thessaloniki, Thessaloniki, Greece; [c]School of Science and Technology, International Hellenic University, Thermi, Greece

ABSTRACT

The mechanical and dynamic behavior of FFF 3D printed polyethylene terephthalate glycol (PETG) and PETG reinforced with 20% carbon fibers is presented in this paper using several experimental tests. Compression tests, cyclic compression tests, nanoindentation, and modal tests were used as the assessment procedures. The results reveal that the addition of carbon fibers decrease as much as 66% the compressive strain, while increase the modulus and the hardness by around 30 and 27%, respectively. The loss factor and damping as calculated from the cyclic compression and models tests dropped from 17.3 to 15.4% and 13.8 to 12.3%, respectively.

KEYWORDS
Additive manufacturing; carbon fibers; mechanical properties; PETG

GRAPHICAL ABSTRACT

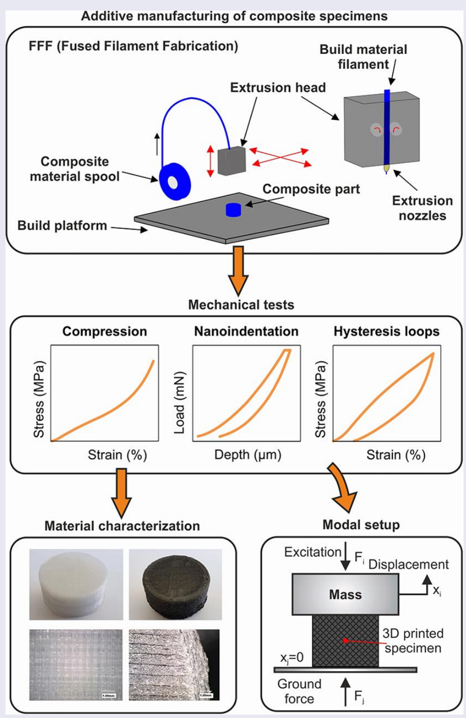

Introduction

Due to global competition and product mass customization, the manufacturing industry is now under more pressure to look for and take advantage of processes that can provide flexibility and cost savings to cope with small batches and rapid product changes. 3D printing processes have had a tremendous impact on the field of design, in the form of rapid prototyping and toolmaking and, more recently, part production. In recent years, it has progressed rapidly and has been widely used in various manufacturing fields such as aerospace, automobile, biomedical, building and many others.[1–4] This tremendous success could be attributed mainly to its outstanding ability to directly manufacture

CONTACT D. Tzetzis d.tzetzis@ihu.edu.gr School of Science and Technology, International Hellenic University, Thermi 57001, Greece.
Color versions of one or more of the figures in the article can be found online at www.tandfonline.com/lpte.

complex parts without special tools, to greatly reduce material waste, and to significantly reduce the time and cost of manufacturing for novel products and small quantity productions. One of the mostly used technique is the fused filament fabrication (FFF) which uses a thermoplastic filament as a building material. This particular technique has caught hold in the hobbyist and do-it-yourself communities with the availability of low-cost machines that are approaching the part quality capabilities of commercial machines. In FFF the filament is pushed through a heated extrusion nozzle, causing the material to melt and deposited layer-by-layer until a 3D object is created.[5] The effects of an array of processing parameters, such as raster angle, printing speed, layer thickness, etc. on the mechanical properties of FFF 3D printed parts have been well researched as documented in the literature.[6–10]

The vast majority of the materials used in FFF machines are ABS, PLA and Nylon, with bulk strengths between 30 and 100 MPa and elastic moduli in the 1.3–3.6 GPa range with those numbers greatly reduced in printed components.[11] However, recently composite materials have been used in 3D printing processes and novel materials are now fabricated incorporating additives with unique characteristics.[12–15] The FFF 3D printing takes advantage of such novel materials produced by combining the base matrix material with additives in specific concentrations and structures. In particular, short carbon fibers are usually blended with unfilled thermoplastic polymers to improve the properties of the polymer material, and therefore to potentially improve the properties of the 3D printed components. A study from Ning, et al. that[16] investigated the mechanical properties of printed samples with 0–15% carbon fiber contents blended with ABS polymer matrix and revealed that the carbon fibers increased the printed samples' tensile strength up to 22%, the Young's modulus up to 31.6%, and the bending strength up to 11.8%. However, the average tensile strength peaked at 5% of fiber weight content. Also, Ning et al.[17] presented results on the effects of processing parameters, such as print orientations, infill speed, nozzle temperature, and layer thickness on the tensile properties. Another paper from Love et al.[18] showed that filament made from carbon fiber and ABS polymer significantly increases strength and stiffness of FFF 3D printed parts. The composite specimens showed a tensile strength of 70.69 MPa and a stiffness of 8.91 GPa, as compared to 29.31 MPa and 2.05 GPa from unfilled ABS tensile specimens. Additionally, they showed that the addition of carbon fibers decreased the distortion of the printed 3D printed ABS parts. This was due in part to the increased thermal conductivity as compared to unfilled ABS. Moreover, Tekinalp et al.[19] conducted tensile tests with carbon fiber filled ABS filament at various fiber weight contents. The fiber reinforced ABS produced an improved tensile strength and tensile modulus by as much as 115 and 700%, respectively, while they showed that the FFF process produced high fiber alignment along the direction of the print path.

Such studies aim toward the understanding of how well these filaments perform when used in 3D printing and what enhancements are realized when carbon fibers are added to the unfilled polymer. It is critical though that such 3D printed materials might result in a range of unidentified mechanical properties of the final part due to the additive nature of 3D printing, while there is an absence in the literature on the behavior of these systems under alternating or dynamic loads. In the current paper the commercially grade polyethylene terephthalate glycol (PETG) and PETG with short carbon fibers are evaluated using mechanical testing in the form of compression and nanoindentation tests. The compression stress–strain graphs are obtained and the modulus is measured, while from the nanoindentation tests the modulus and the hardness is calculated to determine the reinforcing capability of the carbon fibers in a 3D printed state. The dynamic behavior of 3D printed PETG and carbon-modified-PETG specimens is also investigated in this paper. The dynamic mechanical properties of the carbon-modified-PETG were determined by cyclic compression and modal tests. From the loading–unloading cyclic compression curves the loss factor is calculated. The vibration isolation performance of the 3D printed specimens was assessed through an optimization algorithm for modal analysis and identification of experimentally defined transfer functions. This modal testing method derives modal parameters from the transfer functions (TFs) of the composites by a curve-fitting technique.[6–9] To obtain the modal properties of the materials under study a suitable experimental setup has been designed. Using this set-up, the measurement of a set of experimental transfer functions was achieved through the signal processing of the data acquired from the modal tests. For the accurate determination of the dynamic properties of the 3D printed materials, it was imperative to apply a mathematical model fitting the experimental data of the modal tests. The measured data of the experimental transfer functions were utilized as a correlation parameter to analytical–experimental determined TFs. The procedure for the identification of analytical–experimental transfer functions was performed using a genetic algorithm (GA) by minimizing the difference between the measured data from tests and the calculated response, which is a function of the modal parameters. The final phase of this method was the characterization of the vibration isolation performance of the 3D printed materials by analyzing the resonant frequencies and damping.

Regarding to the contribution of the present study, it is shown a compression characterization and nanoindentation of PETG reinforced with carbon fibers with a comparison to unfilled PETG properties, which are not found in the literature. Moreover, this work presents the cyclic compression testing of 3D printed specimens, which is rarely found in previous works for any printing material. The most usual tests are tensile and flexural which permit to determine tensile stiffness properties. In addition, modal tests are also documented, which are not shown at all in the literature for such 3D printed systems.

Materials and fabrication of 3D printed specimens

The main material that has been used in the current paper is the HDglass™, which is an amorphous and high strength modified PETG. Such material was provided in a filament form from Formfutura (Holland) and it is illustrated in Figure 1a,b as taken from an optical microscope. The HDglass™ is transparent as it is an amorphous filament, which lets 90% of the visible light pass through and has less than 1% haze. However, the CarbonFil™ provided by the same company is a light-weight and noticeably stiff carbon fiber reinforced filament. The CarbonFil™ filament which is illustrated in Figure 1c,d is based upon a blend of an HDglass™ compound reinforced with 20% carbon fibers. Therefore, both materials are comparable with respect to the addition of reinforcing fibers since the base material is the same. Both types of filaments provided excellent 3D prints. All specimens tested in this study were produced on a ZMorph SX FDM open source printer with a 1.75 mm extrusion nozzle. Only system integrated (default) variations of production parameters were used in the comparative analysis. The printing parameters used were: nozzle extrusion temperature of 230°C, heat bed temperature of 60°C, deposition line (layer) height 0.2 mm, deposition line width 0.4 mm, and printing speed of 40 mm/s. Deposition speed was therefore not considered a variable in this study and a constant extrusion velocity was selected for all specimens, based on device parameters (e.g., effective printing range). Also, printing was performed in a standard laboratory without temperature or humidity control. The specimens used were cylindrical and had 29 mm diameter and 12.5 mm height reached with 62 printed layers, as illustrated in Figure 2a,b. The associated microscope images are illustrated in Figure 2c–h which show clearly the direction of FFF line deposition having struts in both 0° and 90° directions from layer to layer. For all specimens four layers were printed on the perimeter to form the outer shell which is typical in FFF prints.

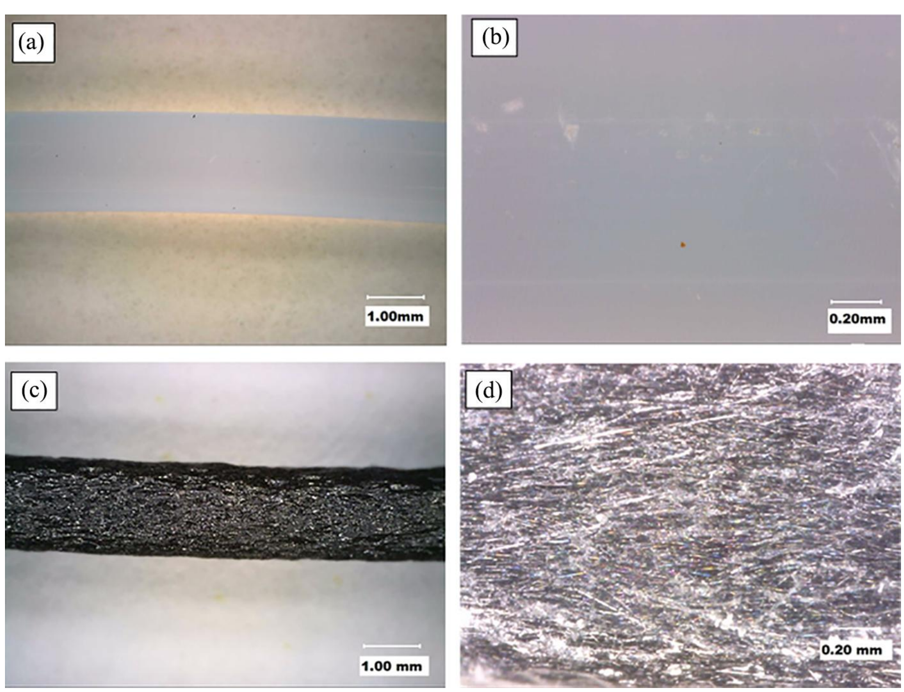

Figure 1. The filaments used for the 3D printing process: (a, b) PETG and (c, d) Carbon microfiber/PETG.

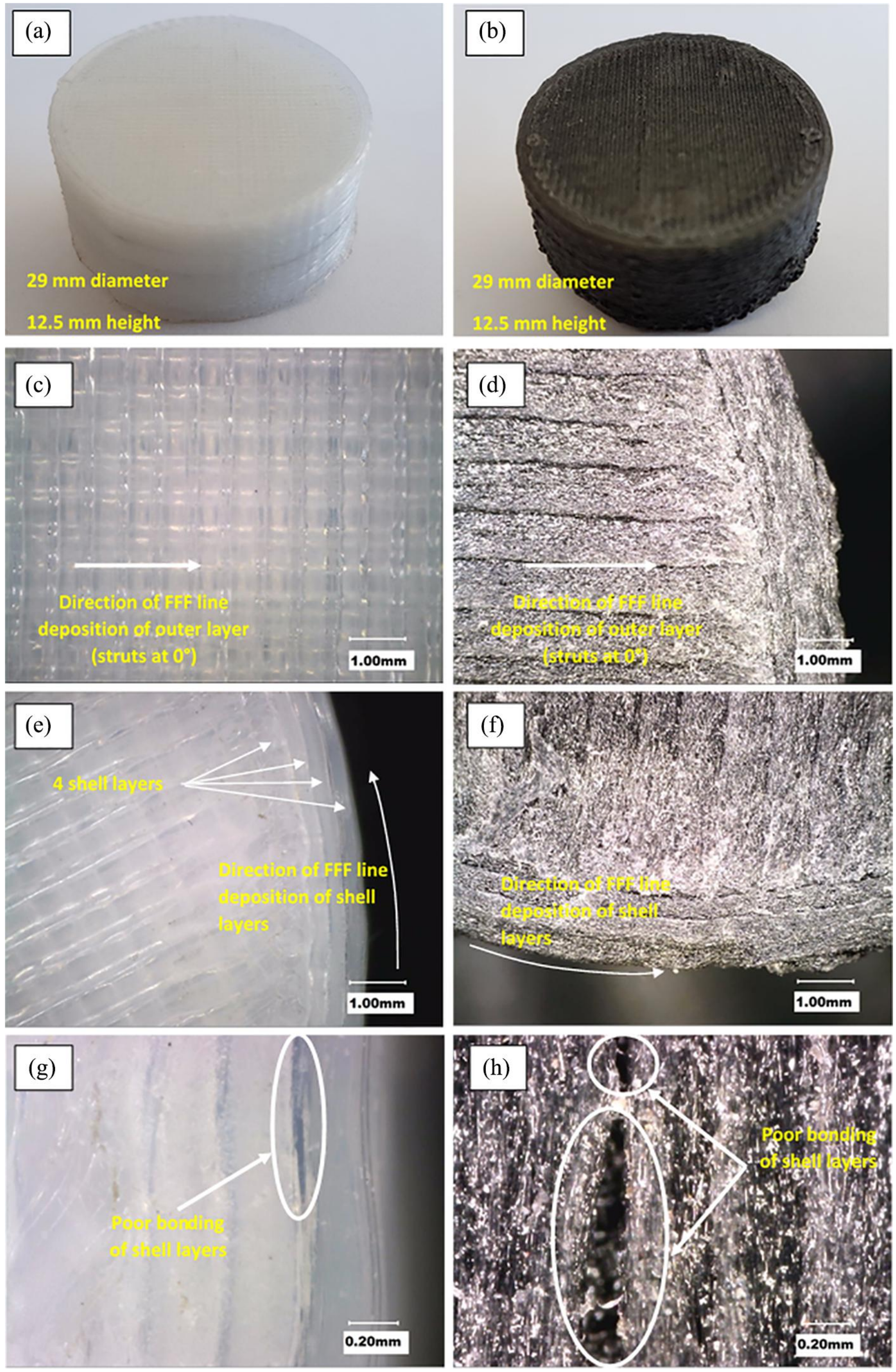

Figure 2. Morphology of PETG (a,c,e,d) and carbon/PETG (b,d,f,h) 3D printed specimens.

Experimental tests

Compression tests

Uniaxial compression tests were conducted using a computer controlled servo-hydraulic single axial test machine, Zwick equipped with a 100 kN load cell. Specimens were compressed between hardened steel compression platens containing a spherical seat to overcome any small misalignment along the load train. Lubrication was applied on the surfaces of both upper and lower platens. The test specimens were placed between the moving head and fixed head of the test machine where the compressive strain in this test reached up to 60% of the original specimen length. The strain rate was set at 5 mm/min and at least five specimens were tested. The stress–strain test was respectively repeated five times for PETG and Carbon/PETG samples.

Nanoindentation test

An alternative technique for the determination of the mechanical properties of polymers is the instrumented indentation technique, which was utilized in the current work. This is a simple but powerful testing technique, which can provide useful information about the mechanical properties of the 3D printed specimens. Various studies have compared the results obtained from nanoindentation instrumented test with the results obtained from the traditional tensile tests especially for the elastic modulus calculation.[20–22] Nanoindentation tests involve the contact of an indenter on a material surface and its penetration to a specified load or depth. Load is measured as a function of penetration depth. Figure 3a shows the typical load and unloading process showing parameters characterizing the contact geometry. This schematic shows a generic viscoelastic–plastic material with the loading OA, and unloading AB′ segments. The plastic work done in the viscoelastic–plastic case is represented by the area W1 (OAB′). The area W2 (ABB′) corresponds to the elastic work recovered during the unloading segment. In the case of purely elastic material, the unloading curve is a straight line (AB) and $h_r = h_{max}$ (W2 = 0). In this case, penetration depth is the displacement into the sample starting from its surface. Further details on nanoindentation experimental techniques on polymers can be found in references.[23–25]

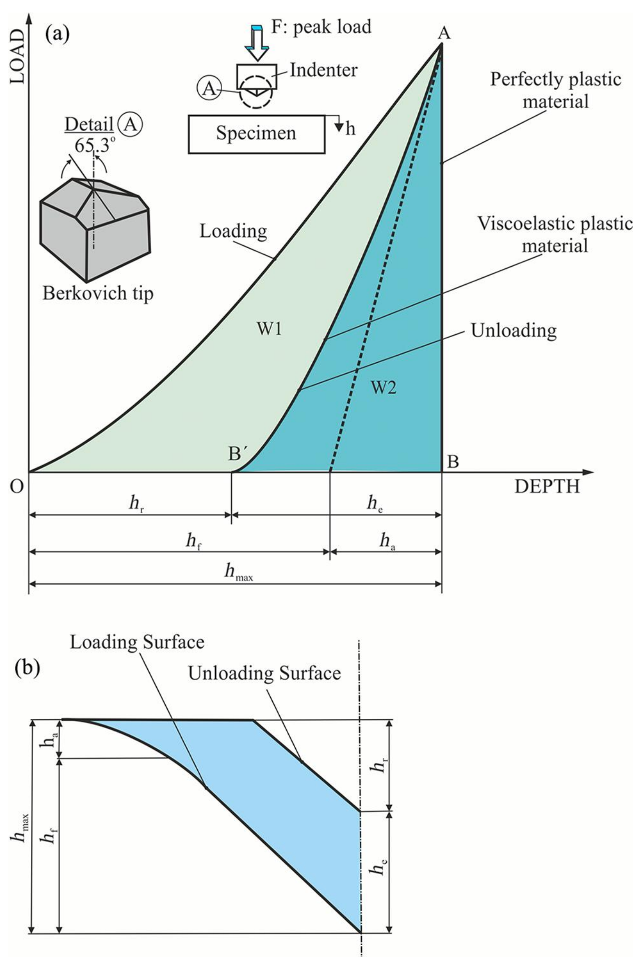

Figure 3. Schematic of (a) indentation load-depth data of a viscoelastic–plastic where h_{max} is the maximum depth, h_e is the elastic depth rebound, h_r is the residual impression depth, h_a is the displacement of the surface at the perimeter and h_f is the contact indentation depth and (b) the loading and unloading surfaces of an indentation (half-section) with the corresponding indentation depths.

In the current work the nanoindentations were conducted on a Fischerscope H100 device, with a resolution of 0.1 mN. The indenter has a Berkovich diamond tip (the tip shape is a three-sided pyramid, with a triangular projected geometry and an included angle of 65.3°; tip radius 20 nm). The nanoindentations made on the surface of the specimens appeared as an equilateral triangle as shown in Figure 3b. On a given specimen, various points were selected with the aid of an optical microscope (which is located in the nanoindenter instrument), under computer control and these were purposely scattered on the surface. In the present case, 40 measurements were conducted on each specimen. Prior to the testing, the indenter area function (that is, the functional relationship between the projected contact area of the indenter and the contact depth) was established through calibration of the instrument, using a fused silica specimen since this material has isotropic material properties.

Prior to an indentation, the indenter was driven, under computer control, toward the specimen surface. After contact, the indenter was driven into the surface, to a depth of around 1.8 μm, at a constant loading rate of 0.35 mN/s, until a peak load of 14 mN was reached and subsequently the indenter was unloaded using the same rate. This peak load was then held for 5 s (to minimize the effect of viscoelastic deformation of the specimen, notably creep, on property measurements) and then the indenter was unloaded, to a load of zero.

The calculation method to determine the modulus and hardness of the materials used for the 3D printed specimens were based on the work of Oliver and Pharr.[26] According to this method, the nanoindentation hardness as a function of the final penetration depth of indent can be determined by:

$$H = \frac{P_{max}}{A} \tag{1}$$

where P_{max} is the maximum applied load measured at the maximum depth of penetration (h_{max}), A is the projected contact area between the indenter and the specimen. For a perfect Berkovich indenter, A can be expressed as a function of the contact indentation depth h_f as:

$$A = 3\sqrt{3}h_f^2\tan^2 65.3 = 24.5h_f^2 \quad (2)$$

The contact indentation, h_f, can be determined from the following expression:

$$h_f = h_{max} - \varepsilon\frac{P_{max}}{S} \quad (3)$$

where ε is a geometric constant $\varepsilon = 0.75$ for a pyramidal indenter, S is the contact stiffness which can be determined as the slope of the unloading curve at the maximum loading point, i.e.,

$$S = \left(\frac{dP}{dh}\right)_{h=h_{max}} \quad (4)$$

The reduced elastic modulus E_r is given by:

$$E_r = \frac{S}{2\beta}\sqrt{\frac{\pi}{A}} \quad (5)$$

where β is a constant that depends on the geometry of the indenter. For the Berkovich indenter, $\beta = 1.034$. The specimen elastic modulus (E_s) can then be calculated as:

$$\frac{1}{E_r} = \frac{1-\upsilon_s^2}{E_s} + \frac{1-\upsilon_i^2}{E_i} \quad (6)$$

where $\varepsilon_{i,s}$, and $\nu_{i,s}$ are the elastic modulus and Poisson's ratio, respectively, for the indenter and the specimen. For a diamond indenter, E_i is 1140 GPa and ν_i is 0.07.

The specimen's hardness H and elastic modulus E_s were obtained from the set of equations given above.

Cyclic compression tests

Steady state, strain rate-controlled cyclic compression tests at ambient temperature were performed with constant strain rates in loading and unloading. The measurement was performed using a material testing system (Testometric, UK equipped with a 50 kN load cell) at a frequency of 0.01 Hz and up to a 5 kN load. The loss of energy in each cycle was calculated from the hysteresis loop. In the quasi-static regime, the stress–strain behavior during loading and unloading was obtained and each polyurethane demonstrated hysteresis behavior. The loading and unloading speeds were set constantly at 5 mm/min. At least five 3D printed specimens were tested under the cyclic compression loading regime. The cyclic compression 3D printed specimens had the same dimensions with the compression tests.

Modal tests

A typical experimental apparatus to evaluate the vibration isolation performance of the 3D printed composite specimens is illustrated in Figure 4, where a 3D printed specimen is mounted on a dynamometer with a cylindrical steel mass (1 kg) used as a static preload. The 3D printed composite specimen provides the stiffness and damping for the SDOF system. An impact hammer with a high-quality piezoelectric force transducer (Endevco Model 2302-10) was used to apply force (input signal) along the center of the mass. The transmitted force was measured with a Kistler 9257A three component piezoelectric dynamometer and an associated charge amplifier. The dynamometer was secured to a heavy granite block by screws to resemble clamped boundary conditions. Simultaneously, the vibratory response (output signal) was recorded through an acceleration transducer with a sensitivity of 100 mV/g (Brüel & Kjaer 4507B), mounted at the top of the steel mass, while the sensing cables were kept in a free state, thereby having a little influence on the vibration tests. The analog signals of the impact hammer, the dynamometer and the accelerometer were amplified and then acquired by an analog-to-digital converter connected to a computer using Matlab software for immediate signal processing. The frequency span of acceleration signals was up to 1600 Hz, the sampling time was 1 s and the sampling frequency was 4096 samples per second (Hz). So the FFT resolution for a block size of 4096 samples is 1 Hz. The modal hammer was calibrated by adjusting the level of the signal trigger force. Each specimen was tested 10 times and linear averaging was performed to cancel the effect of random noise.

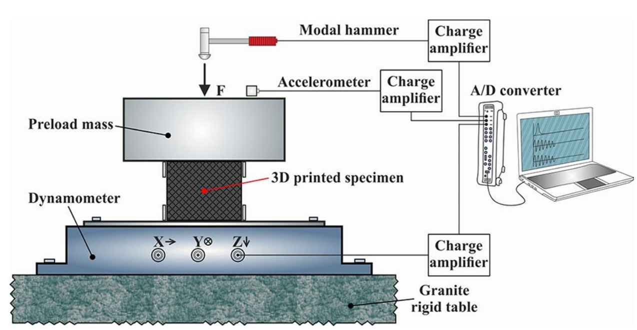

Figure 4. Experimental setup of modal tests for measuring the resonant frequencies and damping of 3D printed specimens.

A specimen with a preload mass can be represented as a single degree of freedom (SDOF) mass-spring-dashpot system. The transfer function G_{ij} characterizes the relation between input excitation at point i and output response at point j of the system. For analytical mode characterization, a genetic algorithm (GA) optimization technique has been used to fit experimental transfer function data with a set of superimposed, single-mode response functions.[27–31] The vibratory response can be calculated in terms of displacement, velocity or acceleration and as a result different terms have been used for the ratios of response to excitation. The ratio of the displacement response to the applied force expresses the receptance (dynamic compliance) of the system.

Results and discussion

Morphology and mechanical properties of the 3D printed composites

The morphology of a neat PETG and a Carbon/PETG 3D printed specimens were studied using scanning electron microscope (SEM) JEOL JSM-840A and the results are shown in Figure 5. PETG shows a typical local thickening effect when a strut at 0° direction is printed on lower layered 90° direction strut. Clearly, the insertion of carbon fibers had a profound effect on the overall microscopic appearance and surface texture of the 3D printed samples. The SEM of the Carbon/PETG material revealed that the fibers were mostly aligned with the length of the 3D printing filament, inside this feeding material, and remained aligned with the direction of printing within the specimens produced by FFF. Also, within the carbon/PETG struts a significant portion of elliptical pores is revealed. The increased porosity of such specimens is attributed to the FFF processing stage. Many of these pores exceed the 20–200 μm in the long diameter of the elliptical shape suggesting that they are not a consequence of any fiber pull-out but probably from adjacent fiber detachment during 3D printing deposition. These pores could behave as stress concentrators during testing, which would probably contribute to lowering the durability of the samples.

There is a marked difference of stress–strain curves under uniaxial compression between the unfilled and carbon fiber filled polymer of as shown in Figure 6. For the same stress, it is found that the corresponding strain of the composite is 66% lower than that of neat PETG. Evidently, as shown in Table 1, the modulus of pure PETG was calculated 2671 MPa and it was improved by the addition of the carbon fibers up to 3482 MPa. Overall, this trend can be profoundly attributed to the softness of the polymer chain structure of neat PETG and the stiffness of the carbon fibers.

Nanoindentation test results are also presented in Table 1 while, typical indentation load–penetration depth curves of the materials under study are shown in Figure 7. The indentation load-penetration depth

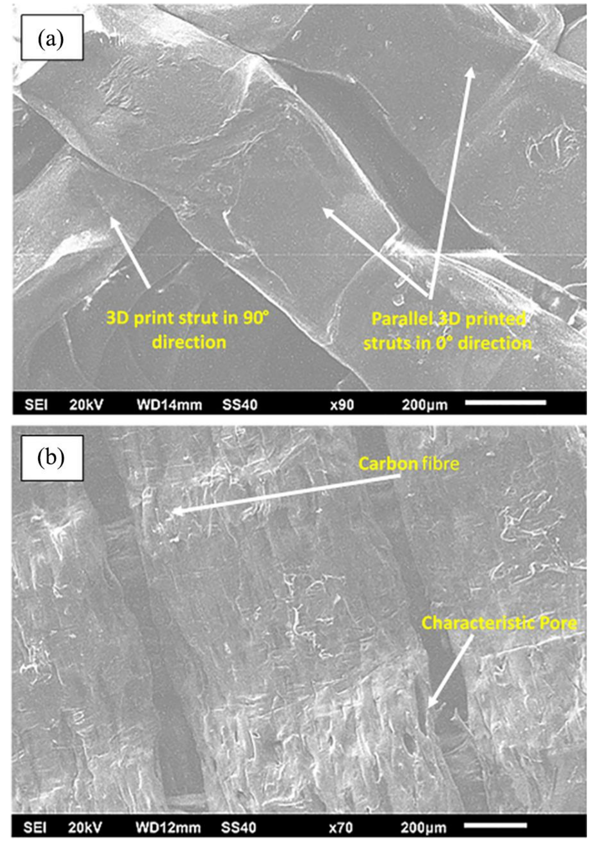

Figure 5. Scanning electron micrographs of (a) PETG showing the typical the local thickening effect when a strut at 0° direction is printed on a bottom 90° direction strut and (b) carbon fiber/PETG parallel struts revealing a significant portion of elliptical pores probably from debonding of carbon fibers during the extrusion process.

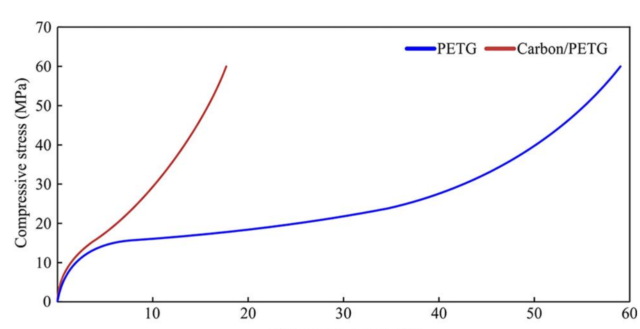

Figure 6. Stress–strain curves of PETG and carbon/PETG specimens.

Table 1. Compressive and nanoindentation properties of the PETG and Carbon/PETG specimens.

	Compression	Nanoindentation	
Specimen	*E*-modulus (MPa)	*E*-modulus (MPa)	Hardness (MPa)
PETG	2671	2619.1	106.2
Carbon/PETG	3482	3413.7	134.9

curves were obtained during indenter loading and unloading. For all samples, the indentation load-penetration depth curves for various indentation peak loads correspond very well with one another, indicating the high accuracy and reproducibility of the indentation method for the studied materials under mechanical load. The indentation load–penetration depth curves for other materials under test indicated creep phenomenon of the specimen at peak load of 14 mN. There were no large differences in creep behavior among the samples while no discontinuities or steps were found on the loading curves, indicating that no cracks were formed during indentation. The indentation depths at the peak load range approximately between 1.7 and 2.2 μm while the carbon PETG curved showed characteristically higher elastic recovery (high elastic deformation). The indentation modulus for the PETG samples was 2619.1 MPa. The addition of carbon fibers increased the modulus to 3413.7 MPa which is approximately 30% increase. These values are directly comparable with the results obtained from the compression tests despite the fact the strain fields in indentation are not uniform, therefore also the strain-rate fields are uniform either; thus, a monotonically direct comparison of rate dependence to compression tests should be assumed with carefulness. As expected the hardness also increased at around 27% with values of 106.2 and 134.9 MPa respectively.

Hysteresis of the 3D printed materials

Under alternating stress, hysteresis occurs when the rate of deformation is less than the rate of stress variation. In this case, since the absorbed and released energies are not balanced in each cycle, the stretching and recoil curve form a closed loop, which is known as a hysteresis loop. The area within the loop represents the energy loss. For polymeric materials, a larger hysteresis loop means higher damping, which more effectively reduces vibration.[32] The damping constants may be derived from the area surrounded by hysteresis loops. Based on the theory of free vibration, the vibration-isolating capacity of materials can be evaluated from the damping constant and the hysteresis damping characteristics.

The specific damping capacity (SDC) is given by:

$$\mathrm{SDC} = \frac{\Delta W}{W} \times 100\% = \left(\oint \sigma d\varepsilon / \int_{\omega t=0}^{\pi/2} \sigma d\varepsilon \right) \times 100\% \tag{7}$$

where σ is the stress, ΔW is the energy dissipated in any one cycle and W is the maximum energy associated with that cycle. The specific damping capacity can be related with the loss factor by:

$$n = \frac{\Delta W}{2\pi W} \tag{8}$$

Figure 8 presents the hysteresis loops curves of 3D printed composite specimens under compressive vibration at 0.1 Hz with an ultimate force of 5 kN. Considering Eqs. (7) and (8), the energy loss over a cycle (ΔW), the maximum energy of that cycle (W) and loss factor (n) were used to measure the material damping of the loading–unloading tests, as shown in Table 2. ΔW indicates that the antivibration property of carbon/PETG material is reduced as compared with the unfilled material. Therefore, the unfilled material is assumed to enhance much better the ability to transform its kinetics to those of thermal dissipation upon the application of an external load. Higher damping constant n, which is the ratio of ΔW to W, is observed

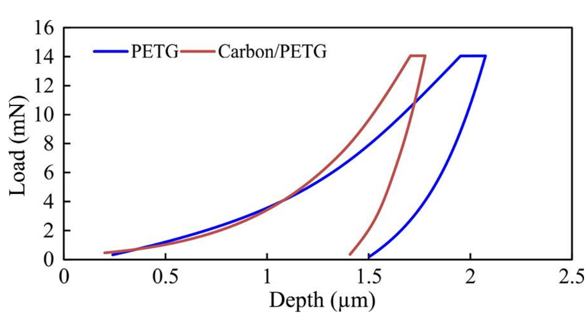

Figure 7. Load–depth profiles of PETG and carbon/PETG specimens.

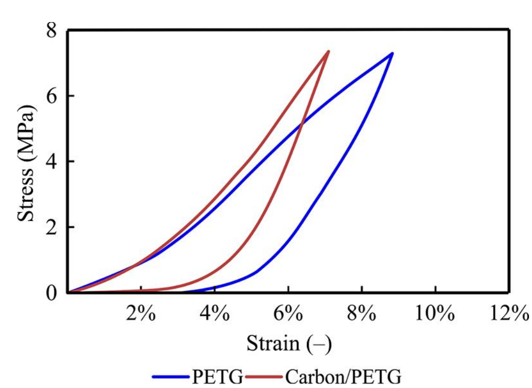

Figure 8. Hysteresis loops of PETG and carbon/PETG specimens.

Table 2. Damping constants of the PETG and carbon/PETG specimens.

Specimen	Area of hysteresis loop, ΔW	Maximum energy, W	Loss factor, n (%)
PETG	0.164051553	0.301701182	17.3
Carbon/PETG	0.099814423	0.206279043	15.4

for neat PETG specimens and this indicates faster energy dissipation at particular amplitudes, which become stable with less vibration. The loss factor for the PETG specimens was calculated 17.3%, while 15.4% for carbon/PETG specimens.

Dynamic mechanical properties of the 3D printed composites

The receptance transfer functions (G_{11}, G_{21}) of the system were calculated in magnitude, real, and imaginary part. These data were then used to calculate the resonant frequencies and the loss factors (n) of each 3D printed-mass system. The data were obtained with curve fitting complex experimental transfer functions through the GA optimization method.[27–31] The analytical transfer functions identified the resonance of the important longitudinal mode for each of the 3D printed specimens. The magnitude of the analytical–experimental receptance functions is shown in Figure 9. The plotted frequency range was selected from 0 to 200 Hz to identify the first axial mode for the 3D printed specimens. The resulted frequency response function (FRF) of each specimen is independent on experimental noise and modal coupling, since each mode of the transfer function was identified separately. The resonant frequencies of the system are indicated by the peak value of the analytical–experimental FRFs as shown in Figure 9. Moreover, the resonant frequency

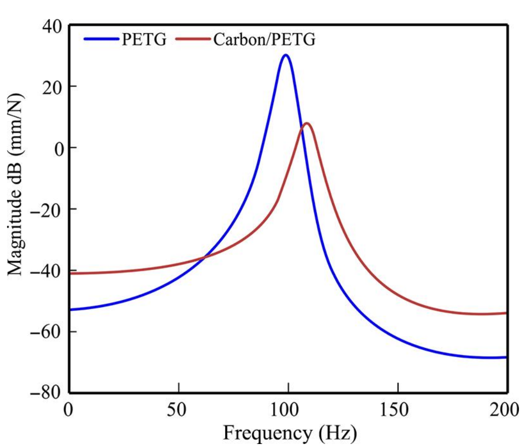

Figure 9. Analytical-experimental FRFs of the PETG and carbon/PETG 3D printed specimens.

Table 3. Modal parameters of the PETG and carbon/PETG 3D printed specimens determined with the transfer function method.

	Modal tests	
	Resonant frequency	Damping (%)
PETG	98	13.8
Carbon/PETG	105	12.3

of the unfilled PETG system is shifted from 98 to 105 Hz in the case of Carbon/PETG. The values of the identified resonant frequencies of the unfilled and carbon fiber filled specimens are shown in Table 3. It is obvious that the frequencies of the fundamental mode increase with respect to the carbon fiber content. This was expected since the carbon fiber addition increases the stiffness of the PETG network due to the higher stiffness of the carbon fibers. Table 3 also shows the values of the damping for the tested 3D printed specimens. Clearly, the addition of carbon fibers in the PETG matrix has not improved the damping behavior. The results in this current work verify the fact that when PETG is loaded with 20 wt% carbon a decrease of around 11% compared with the PETG specimen is attained. These results are in a good agreement with the cyclic compression tests.

Conclusion

This work presents results for mechanical and dynamic testing of commercial materials produced by 3D printing based on FFF. The two printing materials that were investigated, were PETG and PETG reinforced with 20 wt% carbon fibers. The specimens were all printed with direction of FFF line deposition having struts in both 0° and 90° directions from layer to layer with constant microstructure and same build parameters. Also, for all specimens 4 layers were printed on the perimeter to form the outer shell. Optical microscopy revealed certain distinct features especially for the carbon reinforced PETG samples with significant debonded areas between struts and substantial amounts of voids with elliptical shapes in the direction of the FFF deposition. The mechanical properties of the materials under study were investigated initially with static and cyclic compression. As expected the compressive strain of the unfilled PETG was higher than the one with carbon fibers, while the compressive modulus was higher for the carbon/PETG material. Cyclic compression test results showed higher loss factor values for the PETG specimens, which indicated faster energy dissipation at particular amplitudes; they become stable with less vibration. Also, the inclusion of carbon fibers in PETG resulted in moderate reduction of the damping capacity.

ORCID

D. Tzetzis http://orcid.org/0000-0001-5006-5759

References

[1] Kumar, L. J.; Krishnadas Nair, C.G. Current Trends of Additive Manufacturing in the Aerospace Industry: in Advances in 3D Printing & Additive Manufacturing Technologies, Wimpenny, D.I., Pandey, P. M., Kumars, L. J., Eds.; 2017; 39–54, Springer.

[2] Zadpoor, A. A.; Malda, J. Additive Manufacturing of Biomaterials, Tissues, and Organs Ann. *Biomed. Eng.* **2017**, *45*(1), 1–11. DOI: 10.1007/s10439-016-1719-y.

[3] Biswas, K.; Rose, J.; Eikevik, L.; Guerguis, M.; Enquist, P.; Lee, B.; Love, L.; Green, J.; Jackson, R. Additive Manufacturing Integrated Energy-Enabling Innovative Solutions for Buildings of the Future. *J. Energy Eng.* **2016**, *139*(1), 015001. DOI: 10.1115/1.4034980.

[4] Guo, N.; Leu, M. C. Additive Manufacturing: Technology, Applications and Research Needs. *Front. Mech. Eng.* **2013**, *8*(3), 215–243. DOI: 10.1007/s11465-013-0248-8.

[5] Torrado Perez, A.; Roberson, D.; Wicker, R. Fracture Surface Analysis of 3D-Printed Tensile Specimens of Novel ABS-Based Materials. *J. Failure Anal. Prev.* **2014**, *14*(4), 343–353 DOI: 10.1007/s11668-014-9803-9.

[6] Tandon, G. P.; Whitney, T. J.; Gerzeski, R.; Koerner, H.; Baur, J. Process Parameter Effects on Interlaminar Fracture Toughness of FDM Printed Coupons. *Mech. Comp. Multi-Funct. Mater.* **2017**, *7*, 63–71. DOI: 10.1007/978-3-319-41766-0_8.

[7] Tian, X.; Liu, T.; Yang, C.; Wang, Q.; Li, D. Interface and Performance of 3D Printed Continuous Carbon Fiber Reinforced PLA Composites. *Comp. Part A Appl. Sci. Manuf.* **2016**, *88*, 198–205. DOI: 10.1016/j.compositesa.2016.05.032.

[8] Türk, D.-A.; Brenni, F.; Zogg, M.; Meboldt, M. Mechanical Characterization of 3D Printed Polymers for Fiber Reinforced Polymers Processing. *Mater. Des.* **2017**, *118*, 256–265. DOI: 10.1016/j.matdes.2017.01.050.

[9] Zaldivar, R. J.; Witkin, D. B.; McLouth, T.; Patel, D. N.; Schmitt, K.; Nokes, J. P. Influence of Processing and Orientation Print Effects on the Mechanical and Thermal Behavior of 3D-Printed ULTEM® 9085 Mater. *Addit. Manuf.* **2017**, *13*, 71–80. DOI: 10.1016/j.addma.2016.11.007.

[10] Huang, B.; Singamneni, S. Raster Angle Mechanics in Fused Deposition Modelling. *J. Comp. Mater.* **2015**, *49*(3), 363–383. DOI: 10.1177/0021998313519153.

[11] Tymrak, B.; Kreiger, M.; Pearce, J. Mechanical Properties of Components Fabricated with Open-Source 3-D Printers Under Realistic Environmental Conditions. *Mater. Des.* **2014**, *58*, 242–246. DOI: 10.1016/j.matdes.2014.02.038.

[12] Campbell, T. A.; Ivanova, O. S. 3D Printing of Multifunctional Nanocomposites. *Nano Today.* **2013**, *8*(2), 119–120. DOI: 10.1016/j.nantod.2012.12.002.

[13] Compton, B. G.; Lewis, J. A. 3D-Printing of Lightweight Cellular Composites. *Adv. Mater.* **2014**, *26*(34), 5930–5935. DOI: 10.1002/adma.201401804.

[14] Chizari, K.; Arjmand, M.; Liu, Z.; Sundararaj, U.; Therriault, D. Three-Dimensional Printing of Highly Conductive Polymer Nanocomposites for EMI Shielding Applications. *Mater. Today Commun.* **2017**, *11*, 112–118. DOI: 10.1016/j.mtcomm.2017.02.006.

[15] Yang, Y.; Chen, Z.; Song, X.; Zhang, Z.; Zhang, J.; Shung, K. K.; Zhou, Q.; Chen, Y. Biomimetic Anisotropic Reinforcement Architectures by Electrically Assisted Nanocomposite 3D Printing. *Adv. Mater.* **2017**, *29*(11), 1–8 DOI: 10.1002/adma.201605750.

[16] Ning, F.; Cong, W.; Qiu, J.; Wei, J.; Wang, S. Additive Manufacturing of Carbon Fiber Reinforced Thermoplastic Composites using Fused Deposition Modeling. *Comp. Part B: Eng.* **2015**, *80*, 369–378. DOI: 10.1016/j.compositesb.2015.06.013.

[17] Ning, F.; Cong, W.; Hu, Y.; Wang, H. Additive Manufacturing of Carbon Fiber-Reinforced Plastic Composites using Fused Deposition Modelling: Effects of Process Parameters on Tensile Properties. *J. Comp. Mater.* **2017**, *51*(4), 451–462. DOI: 10.1177/0021998316646169.

[18] Love, L. J.; Kunc, V.; Rios, O.; Duty, C. E.; Elliott, A. M.; Post, B. K.; Smith, R. J.; Blue, C. A. The Importance of Carbon Fiber to Polymer Additive Manufacturing. *J. Mater. Res.* **2014**, *29*(17), 1893–1898. DOI: 10.1557/jmr.2014.212.

[19] Tekinalp, H. L.; Kunc, V.; Velez-Garcia, G. M.; Duty, C. E.; Love, L. J.; Naskar, A. K.; Blue, C. A.; Ozcan, S. Highly Oriented Carbon Fiber Polymer Composites via Additive Manufacturing. *Comp. Sci. Technol.* **2017**, *105*, 144–150. DOI: 10.1016/j.compscitech.2014.10.009.

[20] Mansour, G, Tzetzis, D.; Bouzakis, K. D. A Nanomechanical Approach on the Measurement of the Elastic Properties of Epoxy Reinforced Carbon Nanotube Nanocomposites. *Tribol. Ind.* **2013**, *35*, 190–199.

[21] Tzetzis, D.; Mansour, G.; Tsiafis, I.; Pavlidou, E. Nanoindentation Measurements of Fumed Silica Epoxy Reinforced Nanocomposites. *J. Reinf. Plast. Compos.* **2013**, *32*, 160–173. DOI: 10.1177/0731684412463978.

[22] Mansour, G.; Tzetzis, D. Nanomechanical Characterization of Hybrid Multiwall Carbon Nanotube and Fumed Silica Epoxy Nanocomposites. *Polym. Plast. Technol. Eng.* **2013**, *52*, 1054–1062. DOI: 10.1080/03602559.2013.769581.

[23] VanLandingham, M. R. Review of Instrumented Indentation. *J. Res. NIST* **2003**, *108*, 249–265. DOI: 10.6028/jres.108.024.

[24] Briscoe, B. J.; Fiori, L.; Pelillo, E. Nano-Indentation of Polymeric Surfaces. *J. Phys. D Appl. Phys.* **1998**, *31*, 2395–2405 DOI: 10.1088/0022-3727/31/19/006.

[25] VanLandingham, M. R.; Villarrubia, J. S.; Guthrie, W. F.; Meyers, G. F. Nanoindentation of Polymers: An Overview. *Macromol. Symp.* **2001**, *167*, 15–43 DOI: 10.1002/1521-3900(200103)167:1<15::aid-masy15>3.0.co;2-t.

[26] Oliver, W. C.; Pharr, G. M. An Improved Technique for Determining Hardness and Elastic-Modulus using Load and Displacement Sensing Indentation Experiments. *J. Mater. Res.* **1992**, *7*, 1564–1583 DOI: 10.1557/jmr.1992.1564.

[27] Mansour, G.; Tsongas, K.; Tzetzis, D. Modal Testing of Nanocomposite Materials Through an Optimization

Algorithm. *Measurement* **2016**, *91*, 31–38. DOI: 10.1016/j.measurement.2016.05.032.

[28] Mansour, G.; Tsongas, K.; Tzetzis, D. Investigation of the Dynamic Mechanical Properties of Epoxy Resins Modified with Elastomers. *Compos. Part B Eng.* **2016**, *94*, 152–159. DOI: 10.1016/j.compositesb.2016.03.024.

[29] Mansour, G.; Tsongas, K.; Tzetzis, D. Modal Testing of Epoxy Carbon–Aramid Fiber Hybrid Composites Reinforced with Silica Nanoparticles. *J. Reinf. Plast. Compos.* **2016**, *35*(19), 1401–1410. DOI: 10.1177/0731684416652488.

[30] Mansour, G.; Tsongas, K.; Tzetzis, D.; Tzikas, K. Dynamic Mechanical Characterization of Polyurethane/Multi-Walled Carbon Nanotube Composite Thermoplastic Elastomers. *J. Polym. Plast. Technol. Eng.* **2017**, *56*(14), 1505–1515. DOI: 10.1080/03602559.2016.1277243.

[31] Tsongas, K.; Tzetzis, D.; Mansour, G. Mechanical and Vibration Isolation Behaviour of Acrylonitrile-Butadiene Rubber/Multi-Walled Carbon Nanotube Composite Machine Mounts. *Plast. Rubber Compos.* **2017**, *46*(10), 458–468. DOI: 10.1080/14658011.2017.1391975.

[32] Piersol, A. G.; Paez, T. L. *Harris' Shock and Vibration Handbook*, 6th ed; Mcgraw-Hill: New York, 2009.